Specification conformance, grid resolution and inter-code spread in an independent simulation of the SPE11B CO_2 storage benchmark

André Brasil Vieira Wyzykowski
SENAI CIMATEC University, Salvador, Bahia, Brazil
andre.wyzykowski@fieb.org.br abvwmc@gmail.com
ORCID: 0000-0002-2279-4177

This manuscript is a non-peer-reviewed preprint submitted to EarthArXiv.

Abstract. Confidence in geological CO_2 storage forecasts rests on simulators whose discrepancies are, for the most part, characterised against each other rather than against a truth. We wrote a two-phase, two-component, fully implicit CO_2 storage simulator from scratch, ran it on the SPE11B benchmark to the specification's own reporting resolution (840×120 cells, 1,000 yr), and used the reimplementation as an instrument for asking where the discrepancy against the 32 archived submissions comes from. A clause-by-clause reading of the specification against the code found 7 conformance defects, none of which the verification suite — 465 assertions including analytical solutions checked to machine precision — could have detected, because every test encoded the same reading as the code. Repairing 6 of them at fixed grids moved the run 9 and 10 of 54 sampled quantity–time pairs further inside the peer envelope, a measure that cannot be improved by becoming more typical; grid refinement at matched conformance moves that count by less. Because both conformance stages were run at all four grids, the stage change and the resolution change are separated rather than confounded: the largest per-quantity stage effect decays monotonically from 0.88 to 0.03 MAD as the grid refines, and its aggregate, which changes sign twice across the ladder, ends at -0.01 MAD at the reporting grid. Two measured floors calibrate that — a change of time-step policy alone moves the aggregate by 0.46 MAD on identical physics, and a tenfold-finer injection step by 0.06 MAD, more than the finest refinement buys. Separately, a silent clamp on the dissolved-CO_2 mass fraction inside the Newton loop created a false convergence wall: it capped the time step at 0.095 yr and consumed 52% of wall-clock time in discarded iterations while every gate stayed green. Of 18 performance interventions measured by isolated paired A/B, 8 survived and 4 first reported the wrong sign. On the Sleipner benchmark model, at a single fixed resolution, five reduced models scored against the observed top-sand plume outline exceed a matched-area baseline by at most 0.035 in overlap — so which mechanism a model represents separates them less than an explicit baseline reveals. On the benchmark, where both axes were varied, the larger discrepancy shifts came from what the model was asked to represent rather than from how finely it was resolved. Benchmark reporting should require conformance to be demonstrated rather than assumed.

Keywords: CO_2 storage; SPE11; benchmarking; inter-code comparison; code verification; specification conformance; grid convergence; Sleipner

---

1 Introduction

Geological storage of CO_2 is forecast by simulation over centuries, on evidence that is sparse at the time a decision must be made. The forecasts underwrite site selection, permitting and

long-term liability, so their credibility rests on a chain of arguments about where the error in a simulation comes from and how large it is.

That chain has a weak link. Because a thousand-year forecast has no measurable outcome, simulator credibility rests on comparison between codes. The comparative solution project is the standard instrument: a specification is published, independent groups implement it, and the spread of the results is taken as a measure of the uncertainty attributable to implementation (Class et al., 2009; Nordbotten et al., 2024). The eleventh SPE project (SPE11) published its full set of archived submissions (Flemisch et al., 2025a,b), which makes the spread inspectable submission by submission.

The instrument measures spread. It does not, by itself, say what produces the spread. A submission can differ from its peers because it discretises differently, because it converges to a different tolerance, because it uses a different correlation — or because it implements a different problem from the one the specification describes, which is the possibility the exercise is least equipped to detect. Once a code and its tests share a reading of the specification, that reading is invisible from inside.

This paper reports what an independent reimplementation revealed about that question. We wrote a two-phase, two-component, fully implicit CO_2 storage simulator from scratch, without reference to an existing code base, and took it through SPE11B to the specification's own reporting resolution. The purpose is not to add a submission but to use the reimplementation as an instrument: building a code independently and then reading the specification against it exposes the class of error that inter-code comparison cannot see.

What that exercise found runs against the intuition that guided our own effort, and we report it as one code's experience rather than as a field-wide result. A clause-by-clause reading of the specification against the code found 7 conformance defects that the verification suite — 465 assertions including analytical solutions checked to machine precision — could not have detected. Repairing 6 of them at fixed grids moved the run 9 and 10 sampled quantity–time pairs further inside the peer envelope, and moved a leave-one-out consensus distance by 1.85 and 0.72 MAD; grid refinement at matched conformance moves both by less. Both conformance stages have now been run at all four grids, so the two effects are separated rather than confounded, and two measured floors say how much of what remains is the metric rather than the physics.

The paper makes eight contributions, and the conclusions report against this list in the same order.

1. It separates specification conformance from grid resolution as contributors to inter-code discrepancy, using a grid-by-stage matrix in which the stage effect is measured at all four resolutions (Sections 4.1 and 4.2).
2. It calibrates that comparison against two properties of the consensus measures themselves: a time-step-policy floor of the same size as the refinement effects, and a median aggregate that can move against the bulk of its own components in either direction (Sections 4.1 and 4.2.1).
3. It sets out why code verification cannot establish specification conformance when the tests share the code's reading of the specification, and what an itemised clause-to-code review finds instead (Sections 3.2 and 4.1).
4. It identifies a mechanism by which a silent variable clamp presents as a convergence limit while every verification gate stays green, with the diagnostic signature that distinguishes it from a numerical one (Section 4.3).
5. It reports a measurement protocol for simulator performance claims and the 18 interventions it was applied to, including the 10 rejections and the 4 results that first came out with the wrong sign (Sections 3.4 and 4.4).

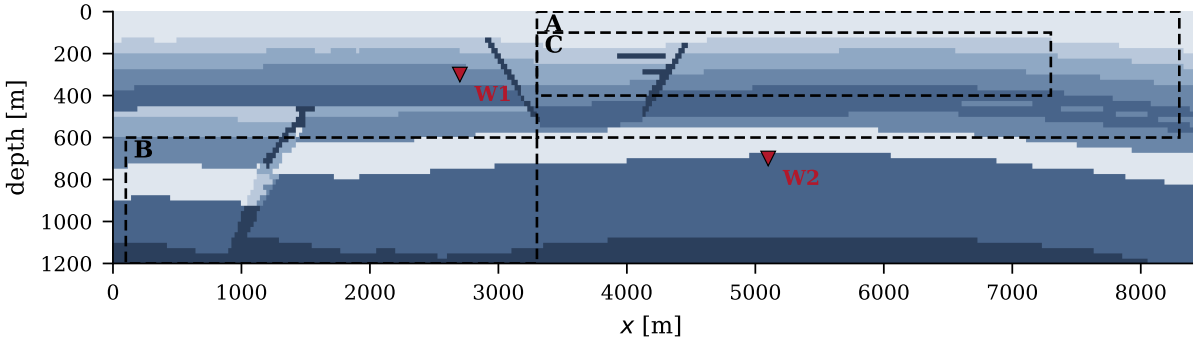

Figure 1: The SPE11B domain as our implementation builds it: seven facies (light to dark with decreasing permeability), the two injectors W1 and W2, and the three reporting boxes A, B and C of the specification. Our facies assignment agrees with the benchmark's reference geometry in all 100800 cells of the reporting grid.

6. It reports what the reporting-grid run produces spatially over the full 1,000 yr: the free-gas footprint does not freeze when injection stops but peaks and then contracts, and a per-column interface metric dates the onset of resolved convective redistribution (Section 4.5).
7. It documents the simulator: a verified code whose capabilities each carry an analytical or published reference solution, of which SPE11B exercises a subset (Section 3.1, Appendix G).
8. And it applies a null-calibrated footprint comparison to a field data set, where five single-mechanism reduced models are scored against the observed Sleipner plume outline at matched area (Section 5).

Everything numerical in this paper is recomputed from the archived data by a generator that the manuscript's build gate runs, and a numeric literal written into the running text fails that gate. That discipline follows the reproducible-research tradition of Claerbout and Karrenbach (1992); Donoho (2010); Peng (2011), and it is not cosmetic here: the single most persistent error in this project was a number that was correct when written and quietly outlived its source.

2 The benchmark and the comparison basis

2.1 SPE11B

The eleventh SPE Comparative Solution Project (Nordbotten et al., 2024) poses a CO_2 storage problem in three variants; variant B is a two-dimensional vertical cross-section at reservoir conditions, 8,400 m wide and 1,200 m deep, containing seven facies arranged into an anticline cut by two faults (Fig. 1). Two injectors operate for the first 50 yr; the simulation continues to 1,000 yr. Before injection begins the specification prescribes an equilibration period of 1000 yr during which the domain reaches thermal and gravitational steady state under the prescribed boundary conditions.

Participants report two products. *Sparse* data are thirteen scalar time series. They comprise pressures at two observation points; mobile, immobile, dissolved and seal-resident CO_2 in each of Boxes A (the anticline crest) and B (the adjacent structural low); a convection-front measure in Box C; total CO_2 in the seal facies; and the mass that has left through the lateral boundaries. *Dense* data are spatial maps on a prescribed 840×120 grid of 100800 cells. The mobility partition is not a modelling choice but a definition given by the specification, and it is one of the places where a plausible reading and the correct reading differ (Section 3.2).

2.2 What "accuracy" can mean without a truth

SPE11B has no analytical or experimental reference. Accuracy is therefore undefined, and any claim that one submission is more correct than another is unsupported. What *is* defined is the position of a result within the distribution the community produced. We use two peer-derived measures of our own, both computable from the archived submissions alone — introducing the weaker one first, because it is the one under which this paper's result is clearest — and report our position under the published SPE11 measure alongside them.

Envelope membership. For each of 9 reported quantities and each of 6 reporting times — 54 pairs — we ask whether our value falls inside the peer group's min–max range. The criterion is blunt: it records no degree of agreement, and a submission at the edge of the spread scores the same as one at its centre. In exchange it has a property no averaged measure has: it cannot be improved by moving toward the middle of a distribution, only by entering or leaving the region the community spans at all. A change that makes a submission more typical without making it more conformant cannot raise this count.

Consensus distance. The finer-grained measure is a leave-one-out deviation, robust in form. The formulation below is ours: it is close in spirit to the inter-submission distances of Flemisch et al. (2025a) but is not identical to any published formula, so the ranks it produces are positions under this measure and not positions in the SPE11 exercise. Where a claim in this paper depends on the measure rather than on the data, we say so and give the sensitivity.

Position under the published measure. Because the distinction matters for how a reader should read a rank, we also implemented the SPE11 distance as published (Flemisch et al., 2025a) — a pairwise, injection-weighted L^2 distance in time, rescaled per criterion by the median pairwise distance and aggregated by an arithmetic–geometric mean — and applied it to the same archive. Of its 15 criteria, 9 are computable from the published sparse data; the remaining six compare spatial maps that the archive does not publish for the peer submissions, so what we report is a sparse-only variant and is labelled as such. Under it our submitted run places 19 of 33 at distance 1.22, against 15 of 33 under Eq. (1). Changing one factor at a time attributes +6 places of that gap to which quantities enter and -2 to the distance algebra; with two factors and no interaction term the two necessarily sum to the total, so this is an accounting of the gap rather than a test that the factors are independent. The published criterion set omits the observation pressures, where this run is closest to its peers, and includes two series whose peer scales are degenerate at the reporting times. As a check that the implementation is not simply mis-scaled, it places the submission that Flemisch et al. (2025a) identify as the SPE11B median simulation 3rd among the peers. For each of 9 reported quantities q and each of 6 reporting times $t \in \{25, 50, 100, 200, 500, 1000\}$ yr, we form the leave-one-out deviation of submission s,

$$d_{s,q,t} \;=\; \frac{\left|\, v_{s,q,t} - \operatorname{med}_{r \neq s}\, v_{r,q,t} \,\right|}{\operatorname{MAD}_r\; v_{r,q,t}}, \tag{1}$$

where med and MAD are the median and the median absolute deviation. The submission's score is $D_s = \operatorname{med}_{q,t}\, d_{s,q,t}$, the median over all 54 entries. Scaling by the peer MAD makes quantities with different units and dynamic ranges commensurable; leaving the submission itself out of its own reference prevents a self-consistent outlier from lowering the bar it is measured against. The measure is robust — a single wild quantity cannot dominate — but it is a measure of *typicality*, not of correctness, and Section 4.2.1 shows a case where that distinction is material.

Which quantities enter the metric. Nine of the thirteen series enter Eq. (1): the two pressures, the mobile/immobile/dissolved partition of Box A, mobile and dissolved CO_2 in Box B, the total seal inventory, and the Box C convection measure. Four are excluded, for reasons the data make concrete. The per-box seal series are components of the seal total and would count the same physics twice. Immobile CO_2 in Box B is reported as exactly zero by 69% of peers at the early reporting times, so its peer MAD degenerates and Eq. (1) would turn rounding differences into ranking; the boundary-outflow series degenerates the same way. The choice is not innocent, so we report its sensitivity: rerunning the whole ranking over all thirteen series (with the degenerate scales guarded, and 2 quantity–time cells carrying an exactly zero peer MAD) moves our run from rank 15 of 33 to rank 13, at distance 0.97 against 0.93. The final position does not depend on the selection; the magnitude decomposition of Section 4.1 partly does, and Appendix F extends the sensitivity to every configuration and says exactly which statements survive.

The peer group. The comparison uses the 33 sparse-data files archived for SPE11B (Flemisch et al., 2025b). These are the submissions of the exercise itself, spanning established research and commercial simulators — among them DuMu$^{\mathrm{x}}$, OPM Flow, GEOS, MRST and PFLOTRAN. The 32 usable files come from 17 code families, of which 9 submitted more than one configuration, so the group samples both implementation and setup variability (Flemisch et al., 2025a). Of these, 1 (`csiro1`) does not carry the full column set the specification prescribes and is excluded, leaving 32 usable peers; adding our own run gives 33 ranked entries. We apply no other filter. Archived submissions that are visibly atypical in one quantity or another are retained: the peer group is what the community produced, and trimming it to taste would make the reference a matter of our own judgement.

3 Methods

3.1 The simulator

The model solves two-component (CO_2, H_2O) two-phase flow with a fully implicit formulation, in the compositional reservoir-simulation tradition of Aziz and Settari (1979) and Coats (1980). Mass conservation for component c reads

$$\frac{\partial}{\partial t}\Big(\phi \sum_{\alpha} \rho_\alpha S_\alpha X_\alpha^c\Big) + \nabla \cdot \sum_{\alpha} \Big(\rho_\alpha X_\alpha^c \mathbf{u}_\alpha - \phi S_\alpha \rho_\alpha \mathbf{D}_\alpha \nabla X_\alpha^c\Big) = q^c, \tag{2}$$

with the phase velocity given by the multiphase Darcy law, $\mathbf{u}_\alpha = -\left(k_{r\alpha}/\mu_\alpha\right)\mathbf{K}(\nabla p_\alpha - \rho_\alpha \mathbf{g})$, and an energy equation solved for temperature on the same grid. Fluxes are two-point flux-approximation on a structured grid with harmonic transmissibility averaging; mobilities are upwinded by phase potential, so the upwind direction is decided per phase and per face rather than from the total velocity. Phase appearance and disappearance use primary-variable switching in the manner of Pruess et al. (1999): a cell carries $(p, X_{\mathrm{w}}^{CO_2}, T)$ when single-phase and (p, S_{g}, T) when two-phase, with the switch driven by saturation and by supersaturation of the dissolved component. The Jacobian is assembled analytically where the derivative is available in closed form and by finite difference elsewhere; the linear system is solved by GMRES (Saad and Schultz, 1986) preconditioned with a threshold incomplete LU factorisation (Saad, 1994) (SuperLU's ILUTP, reached through scipy's `spilu`).

Fluid properties follow the specification's prescribed correlations: mutual solubilities from Spycher et al. (2003), brine density from García (2001) with the Setschenow salting-out correction, brine viscosity from Batzle and Wang (1992), and CO_2 density and viscosity from Span and Wagner (1996) and Fenghour et al. (1998). Relative permeability and capillary pressure

follow the Brooks–Corey forms (Brooks and Corey, 1964) the specification fixes per facies, with residual trapping by the Land (1968) relation. Well inflow uses the Peaceman (1978) index.

The numerical settings the results depend on are as follows. Convergence of a Newton step requires the max-norm of each component residual, scaled per cell by pore volume times a reference density over Δt, to fall below 10^{-6}, with at least one linear solve always performed. The time-step controller multiplies Δt by 1.5 when a step converges in at most 4 iterations and by 0.6 when it needs 9 or more, subject to the ceiling $\Delta t_{\max}$ that our production runs pin as an accuracy control (Section 4.4). Jacobian entries without closed-form derivatives use one-sided differences with perturbations of 10 Pa in pressure and 10^{-7} in composition. Phase appearance is triggered by supersaturation of the dissolved component and disappearance by exhaustion of the gas saturation; inside the Newton loop the dissolved mass fraction may go negative by at most 10^{-6} (the tolerance whose absence Section 4.3 is about), with an exact projection applied once at commit and the projected mass counted. Each linear system is row-equilibrated to unit maximum row magnitude, then solved by GMRES with restart 60 to a relative tolerance of 10^{-10}, preconditioned by threshold incomplete LU (ILUTP) with drop tolerance 10^{-8} and fill bound 20. Within a Newton solve the factorisation is reused for up to 40 iterations before a rebuild; every reuse, rebuild and fallback to a direct solve is counted and reported.

The code that produced these results is 9144 lines of Python with NumPy and SciPy, with an optional CuPy backend for assembly, held to 42 verification groups and 465 assertions (Section 3.3). SPE11B exercises a subset of it: the same core also carries an energy equation, reactive transport with mineral kinetics, two-way poromechanics, hysteretic relative permeability, halite precipitation, dual-porosity transfer, fracture conductance and vertical-equilibrium reductions, each gated against an analytical or published reference solution. Table 8 in Appendix G lists them with their oracles and marks which are active here; only the flow, transport and constitutive components in that list bear on the results below, and the claims in this paper are scoped accordingly.

A full 1,000 yr run costs 251 s at 168×24 and 23.4 h at 672×96 on one workstation, the latter over 9194 accepted steps; at the official grid a step costs 5.48 s under the free controller (Appendix D gives the machine and the step anatomy). Section 4.4 treats performance where the measurement revealed something about the numerics.

3.2 Reading the specification against the code

In the standard taxonomy, verification asks whether the equations are solved right and validation whether the right equations are solved (Oberkampf and Trucano, 2002; Roy and Oberkampf, 2011). The failure mode this section documents sits between the two: the code solved, correctly, a faithfully implemented misreading of the specification. The verification suite described in Section 3.3 was in place, passing, and answering the wrong question. Every test it contained compared the code against an independently computable solution — hydrostatic equilibrium, Buckley–Leverett, an analytical aquifer response, bit-exact restart. None of them could detect a case that was set up faithfully to a *misreading* of the specification, because in that case both the code and the test encode the same misreading.

We therefore ran a different exercise: a line-by-line reading of the benchmark description against the code that implements it, taking each numbered equation, table and clause in turn and locating the lines responsible for it. This found 7 discrepancies (Table 1). They are not subtle numerical issues. Two are wrong formulas; one is a factor-of-10 anisotropy; one replaces a per-facies parameter table with a single scalar; one implements a plausible but incorrect reading of a definition; one omits a prescribed initialisation stage.

We record D7 explicitly rather than silently. It is a real deviation from the specification; we measured its consequence, found it negligible at 2.8×10^{-7} of the domain CO_2 inventory, and chose not to repair it. A reader who disagrees with that judgement can see exactly what

Table 1: The 7 discrepancies found by reading the specification against the code. Every one of them was present while the entire verification suite of Section 3.3 passed. D7 is a deviation we chose to keep after measuring its effect; the rest were repaired.

	Specification item	Discrepancy and measured consequence
D1	relative permeability	normalisation applied to the wrong saturation interval; gas relative permeability too large by up to 1.93×
D2	capillary pressure	the prescribed cap was not enforced; capillary pressure in the seal reached 5.7× the permitted maximum
D3	permeability tensor	vertical permeability set equal to horizontal instead of $k_z = 0.1\,k_h$: anisotropy wrong by 10×
D4	dispersion	the per-facies dispersivity table replaced by one scalar
D5	mobile/immobile split	classification by residual saturation rather than the specification's definition; immobile CO_2 in Box A too large by about 100× the peer median
D6	equilibration	the prescribed 1000 yr pre-injection equilibration was not run
D7	vapour composition	equilibrium composition evaluated at the phase's own pressure rather than a common one. *Kept*: measured effect 2.8×10^{-7} of domain CO_2

was traded.

3.3 Verification and gates

Correctness is enforced by two commands. A *golden* test replays a fixed scenario and compares every state variable against a stored reference at $r_{\mathrm{tol}} = 10^{-9}$, giving 0 mismatches and a component mass-balance residual of 3.47×10^{-9}. A *verification* suite runs 42 groups comprising 465 individual assertions, of which 0 fail; these cover analytical solutions, conservation identities, restart reproducibility, and — since this work — the whole benchmark evaluation trajectory of Section 4.1.

Two habits matter more than the counts. First, every claim in this paper that a gate detects something was checked by seeding the defect it is meant to catch and confirming that the number moves: removing the MAD scaling from Eq. (1) — which makes the distance dimensional, so that the largest-magnitude quantities swamp the rest — reports us at rank 8 instead of 15, and halving the width of the peer min–max intervals drops the envelope count from 53 to 44 of 54. Both fault injections are executed by the fact generator itself, so those two numbers are recomputed rather than remembered. A check is trusted here only after it has been shown to fail on a seeded defect. Second, the evaluation pipeline is itself under test: the ranks and envelope counts quoted throughout are recomputed from the archived submissions on every run, not stored.

3.4 How performance was measured

Wall-clock claims follow one protocol, stated here and applied without exception in Section 4.4, which also reports what it rejected. Measurements are *isolated A/B*: the two code paths run in the same process on the same restored simulation state, alternating, with the long-running

production job suspended for the duration. The reported statistic is the median of paired ratios, not the ratio of medians and not the minimum of N; the pair counts, medians and ranges of every deciding run whose pairs were archived are tabulated in Appendix D. Acceptance is mechanical, not judged: an intervention was adopted only when every paired ratio of its deciding run exceeded unity, so a change whose range straddles unity is rejected regardless of its median.

4 Results I: SPE11B

4.1 Conformance dominates

Figure 3 places every configuration we ran by grid size and by the two measures of Section 2.2: its vertical extent is what conformance bought, its horizontal extent what resolution bought.

The envelope count is where the result is cleanest, because it cannot be improved by moving toward the middle of a distribution (Section 2.2). At the coarsest grid (168×24, 4032 cells), held fixed, repairing defects D1–D6 moved it from 38 to 47 of 54 sampled quantity–time pairs; at 336×48, from 42 to 52. Both gains are large and share a sign. Refinement moves this count too (Fig. 2): along the matched D1–D6 ladder it runs 47, 52, 54, 53 of 54 — recovering over the coarse grids what conformance repair had already bought there, then stopping, with the maximum at 672×96 rather than at the finest grid we ran. The consensus distance tells the same story over the same pairs, moving from 3.24 to 1.39 and from 2.25 to 1.53. None of these changes involved touching the discretisation, the solver, the tolerances or the time-step control. They were changes to what the model was being asked to represent.

The coarse post-conformance result (1.39 at 4032 cells) is closer to the peer consensus than the pre-audit result at 16128 cells (2.25): the more conformant configuration on 4× fewer cells sat closer to the group than the less conformant one on more — closer to consensus, not "more correct" (Section 2.2). And none of the 7 defects was detectable by the verification suite of Section 3.3, which was not weak: it was checking analytical solutions to machine precision. The defects survived because a test built from the same misreading as the code agrees with the code.

Distances of this size have to be read against the metric's own reproducibility, which can be measured rather than assumed. Rerunning identical physics at 168×24 under a different time-step policy moves the nine-quantity aggregate by 0.46 MAD (1.39 to 1.85) — as large as the refinement ladders of Section 4.2. All of it is one quantity: `immA` moves +1.65 MAD on its own, and its absolute masses at this grid are tens of tonnes against peer medians of tens of kilotonnes, so its scaled deviation is front-position quantisation noise. No other quantity moves by more than 0.35 MAD, and excluding `immA` the two baselines agree to 0.01 MAD (1.53 against 1.54). The floor is therefore quantity-specific rather than general. It is still not negligible: the aggregate at the coarsest grid carries a policy-dependent term of the same magnitude as the effects Section 4.2 reports. And the archived trajectory — assembled as the work proceeded, not as a designed experiment — does not hold the time-step policy fixed across its rows, which Table 4 now records. Every per-item statement below is given twice, with and without `immA`.

The trajectory bundles the repairs, so it cannot say which item mattered; a per-item battery can, and what it says is not what we expected. At 168×24, each of D1–D5 was re-introduced alone as a reconstructed broken variant — documented in the builder, not a replay of the historical bug — against a matched-policy baseline (Table 7, Appendix E). The reconstructed D5 raises the physical `immA` signature 11.1× at late time and still moves the full aggregate by only +0.08: the median absorbs six entries out of 54 — the same effect this paper reports elsewhere, here inside its own ablation. The attribution itself: only D3, the vertical-permeability anisotropy, is individually costly (+0.46 MAD excluding `immA`); D2 is neutral alone, and D1 alone *improves* the consensus distance (-0.36 MAD) — re-breaking it moves the run toward

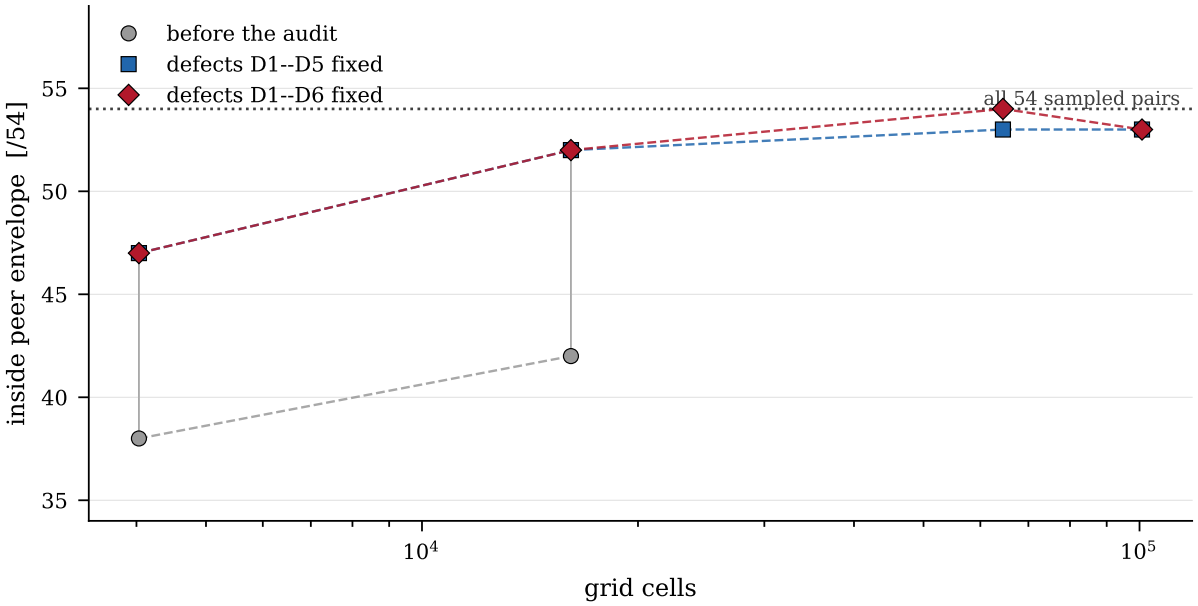

Figure 2: Peer-envelope membership — the count of the 54 sampled quantity–time pairs that fall inside the peer min–max range — for every configuration. Unlike a consensus distance, this count cannot be improved by moving toward the middle of the peer distribution. Solid vertical ties are conformance repair at fixed grid; dashed ties are refinement at fixed conformance stage.

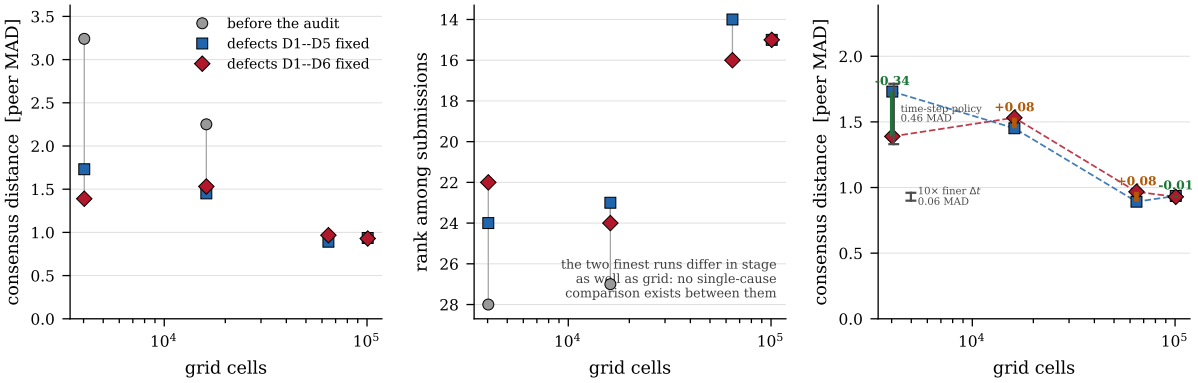

Figure 3: Left and centre: consensus distance and rank among the 33 entries for every configuration, against grid size. Marker shape and colour give the conformance stage; thin grey lines join configurations that share a grid, so a vertical drop is the effect of conformance alone. Right: the same distances with the two effects separated. A vertical bar is the D1–D6 stage effect at that grid, green where it improves the score and orange where it worsens it; dashed lines join configurations at one stage, so their slope is refinement at matched conformance. The two I-beams give the measured floors — a change of time-step policy on identical physics, and a tenfold-finer injection step — drawn at the height of the stage effect each one bounds, so the lengths compare directly. The stage bar shortens with every refinement and is shorter than both floors at the reporting grid.

the group. The five individual deltas sum to +0.03, while the bundled repairs moved this grid by 1.85: the gain was carried by interactions between items and by the mobility repair's effect on a noise-floor quantity, not by per-item additivity. A specification review is a package, and its value cannot be read off item-by-item counterfactuals at a coarse grid.

4.2 Separating conformance from resolution

The specification's own reporting grid is 840×120 (100800 cells), and with both conformance stages now run at every grid, what refinement buys can be read between the same two endpoints

at each stage. Over the full ladder from 168×24 to the official grid — a 5× refinement per axis — the consensus distance improves by 0.8 MAD at D1–D5 and 0.46 at D1–D6, the latter non-monotonically (1.39 → 1.53 → 0.93). Both are smaller than the conformance repairs at fixed grid, which bought 1.85 MAD at 168×24 and 0.72 at 336×48, and the D1–D6 ladder is exactly the size of the 0.46 MAD time-step-policy floor of Section 4.1 — an entire 5× refinement worth no more than changing when the controller is allowed to take a longer step. (These magnitudes are statements about the nine-quantity metric; under the full thirteen-column set the coarse-grid ordering reverses — Appendix F.)

The comparison a reader wants is between the two finest runs, 0.89 at 672×96 against 0.93 at the official grid — a pair that is confounded, because those two runs differ in conformance stage (D1–D5 against D1–D6) as well as in resolution. An earlier version of this work quoted it as a negative result for refinement. Both directions of the confound are now measured separately, because the deconfounding run at 672×96/D1–D6 completes the row.

The stage change, at fixed grid, moves the aggregate by -0.34 MAD at 168×24, +0.08 at 336×48, +0.08 at 672×96 and -0.01 at the official grid — improving the score sharply at the coarsest grid, worsening it at the two middle ones, and returning to near zero at the finest. The aggregate is therefore not monotone in resolution, and we do not present it as such. What is monotone is the size of the change: its largest per-quantity movement falls across all four grids, from 0.88 MAD (in `immA`) through 0.17 and 0.12 to 0.03. Whether the prescribed equilibration was run moves individual quantities by up to 0.88 MAD on a grid too coarse to resolve the front and by 0.03 on the reporting grid; which direction the aggregate moves on the way is not something these four points determine. An earlier version reported the decay at three grids and declined to extrapolate it; the fourth cell, run since, continues it.

Refinement at matched conformance, over that same final step, is 0.04 MAD holding D1–D6 (0.97 to 0.93) against -0.04 holding D1–D5 (0.89 to 0.94) — the same 2×-per-axis refinement worth ±0.04 MAD depending only on which stage it is measured at. The confounded pair therefore decomposes exactly: a stage cost of +0.08 and a matched-refinement gain of 0.04 net the 0.04 MAD deterioration the earlier reading attributed to resolution alone. What that reading got wrong was not the sign of the refinement effect but its size.

Both sides of that decomposition are hundredths of a MAD, so what bounds them matters more than their sign, and both bounds are measured (Table 4 lists every configuration behind these comparisons). Repeating the official configuration with the injection-period time step reduced tenfold moves the aggregate by 0.06 MAD (0.93 to 0.99) — larger than the 0.04 MAD that the final refinement buys. Per quantity the pressures move by at most 0.08%, mobile Box A CO_2 by 1.51% and dissolved Box A CO_2 by 2%; the exception is `immA`, which moves 39.2% at 1,000 yr, worth 0.98 MAD — the same quantity that carries the time-step-policy floor at the coarse grid, behaving the same way at the fine one. (One entry moves further in scaled terms, `dissB` at 25 yr at 3.9 MAD, on a peer scale degenerate enough that Section 2.2 excludes its Box B counterpart for the same reason.) At 0.06 and 0.46 MAD, time-step choice and conformance stage both matter at the scale of the refinement gains: at this resolution, the discretisation is not where the largest gains are.

Envelope membership behaves differently, and more informatively. Over that same final step it goes 53 to 53 of 54 at matched D1–D5, and 54 — every sampled pair — to 53 at matched D1–D6: flat at one stage and down one at the other, with the maximum at 672×96 rather than at the finest grid we ran. Of the official grid's 53, 46 also sit inside the peer P10–P90 band, so the run lies within the bulk of the peer distribution at either resolution. The configuration that achieves full envelope membership is not the finest one, which is the same point the distance decomposition makes from the other side: past the resolution where migration is resolved, further refinement is not what moves this run relative to its peers. The run submitted as this paper's configuration of record remains the one at the specification's own reporting grid.

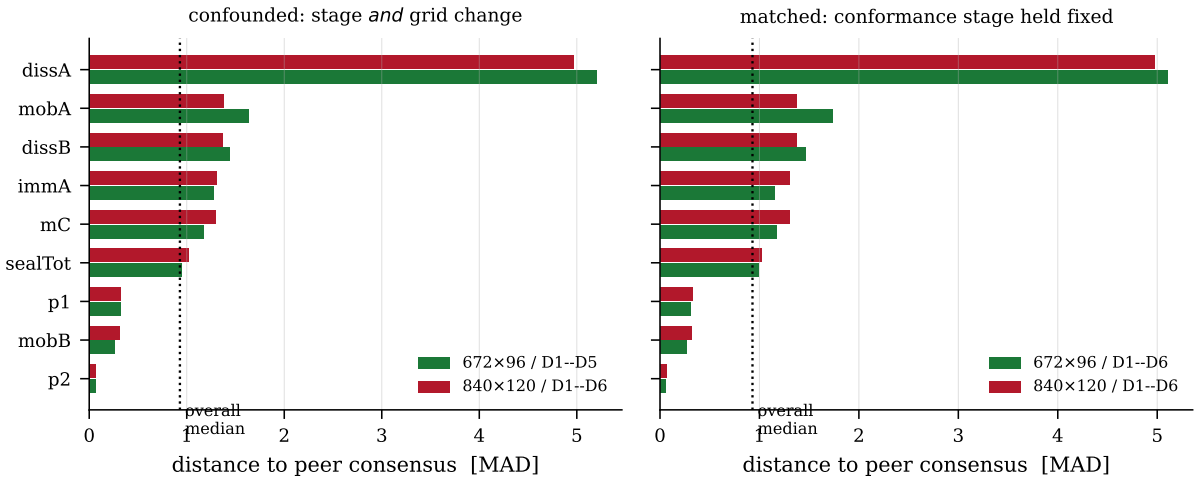

Figure 4: Consensus distance by quantity for two refinements of the same 2×-per-axis step. Left: the confounded finest pair, which differs in conformance stage as well as grid — 5 of 9 quantities move closer to the peer consensus while the median aggregate (dotted line) moves away. Right: the same refinement at matched D1–D6 conformance, where only 3 of 9 improve and the aggregate moves closer. A median over heterogeneous entries can move against the bulk of its components in either direction.

4.2.1 Why a median aggregate can move against its components

The aggregate can move against the bulk of its components, in either direction, and the mechanism applies to any median-based consensus metric. Figure 4 resolves the consensus distance by quantity for the confounded finest pair. Between those two runs, 5 of the 9 quantities improved, including the two furthest from the peer group: `dissA` fell from 5.2 to 4.97 and `mobA` from 1.63 to 1.38. The 4 that degraded (`immA`, `mobB`, `sealTot`, `mC`) did so by between 0.02 and 0.13 MAD, among quantities already close to the group — and the aggregate still got worse, because it is a *median* over 54 entries. Improvements concentrated in the tail move entries that lie far above the median without moving the median itself, while small degradations spread across the middle move it directly. A robust statistic is insensitive to the tail by construction, and here the tail is where the physics improved.

The matched-conformance refinement of Section 4.2 gives the same mechanism with the opposite sign, and gives it without a confound: refining 672×96 to the official grid at fixed D1–D6, only 3 of 9 quantities improve and 6 degrade, yet the aggregate *improves* by 0.04 MAD (Fig. 4, right). The components moving one way while the summary statistic moves the other is therefore not an artefact of the confounded pair; it is what a median over heterogeneous entries does, and it can flatter a configuration as easily as it can penalise one.

The consequence is not confined to this measure. Any leave-one-out consensus statistic of this shape — and the inter-submission distances of Flemisch et al. (2025a) are of this shape — rewards being typical. A configuration can improve where it is furthest from the group and be scored down for it, and a configuration can degrade on most of its quantities and be scored up. Either way the gradient points toward the group rather than toward correctness, which is why Section 6 argues for reporting the distribution alongside any such score.

4.2.2 The largest discrepancy is insensitive to the refinements performed

Dissolved CO_2 in Box A is our furthest quantity from the peer group, at 4.97 MAD. Figure 5 shows it against the peer median at four resolutions. The ratio to the peer median falls as the grid refines and then stops: between 672×96 and the official grid the trajectory changes by at most 2.6%, and both curves hold a median ratio of 1.48× to the peer median across the full 500 yr window. Two caveats bound what that can mean. First, that ladder's final point differs

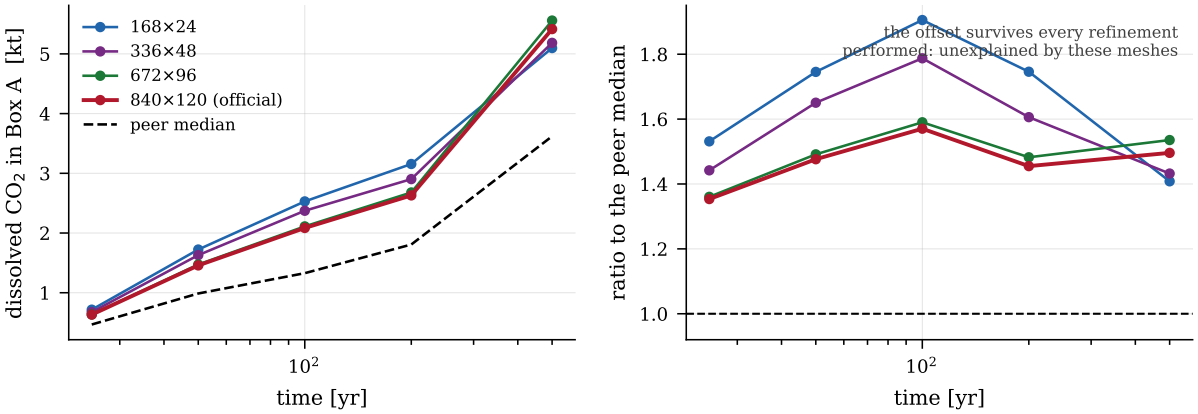

Figure 5: Dissolved CO_2 in Box A at four resolutions, absolute (left) and as a ratio to the peer median (right). The two finest grids collapse onto each other while remaining above the peer median: the discrepancy is insensitive to the refinements performed. The final point differs in conformance stage from the rest of the ladder, and no convergence order is claimed (Section 4.2).

in conformance stage from the rest. The stage change alone moves the `dissA` trajectory by 2.6% at the grid where it is isolated — as much as the total change across the refinement — so the two cannot be separated on this ladder. What can be said instead comes from the matched-conformance comparison: at fixed D1–D6, the per-quantity `dissA` distance moves from 5.1 to 4.97 MAD across the same refinement, which is the same order as the confounded reading and is not confounded. Second, we looked for the precondition that any formal convergence order — a Richardson extrapolant or a grid-convergence index in the sense of Roache (1994) — would require: monotonically shrinking between-grid increments on the matched-conformance ladder. They do not shrink; the increment *grows* from the second refinement to the third at 3 of 5 reporting times. The ladder is not in an asymptotic regime, so we claim insensitivity over the range tested and decline to claim convergence.

A quantity that stops moving under refinement is unexplained by the discretisation changes evaluated — a statement about the tested range, not about the limit. The distinction is material because Landa-Marbán et al. (2026) refine SPE11B far past our finest grid, to sub-metre cells, and report that while observation-point pressures converge robustly even on coarse grids, the phase-partitioning and dissolution measures stay grid-sensitive with no clean convergence pattern. Their result and ours agree where they overlap — pressures are our two best quantities, at 0.32 and 0.06 MAD — and theirs extends beyond our range, so whether the offset would survive sub-metre refinement should not be assumed.

We have not identified the mechanism. Candidates consistent with the evidence include the dispersion treatment, the solubility correlation at the in-situ salinity, and the interaction between the mobility classification and the dissolution front; distinguishing them needs a controlled comparison against another implementation, which one code cannot settle. We report it as an open discrepancy rather than tuning it away, because tuning it away is precisely what a consensus metric rewards and what makes inter-code agreement uninformative.

By contrast, mobile CO_2 in Box B — absent on the coarsest grid — is resolved by 672×96: at 100 yr it reaches 3.01 kt against a peer median of 3.07 kt, and 2.97 kt at the official grid. Box B is a migration problem, and migration needs resolution; Box A dissolution did not respond materially over the range evaluated here. Resolving the physics of a quantity and improving its score are not the same thing: `mobB` is also one of the quantities whose scaled distance degrades slightly across the finest refinement (Fig. 4), because once a quantity is inside the peer spread, further movement is movement relative to a group median rather than toward a truth.

4.3 A silent clamp that looked like a convergence limit

The most consequential defect we found was not in the physics. It was one line inside the Newton loop that clipped negative dissolved-CO_2 mass fractions to zero in single-phase cells — a defensive guard on a variable that is physically non-negative.

Single-phase cells near the dissolution front repeatedly requested a small negative mass fraction, of order -5.616×10^{-7}. The clamp returned them to zero on every iteration. The result was not a wrong answer; it was a fixed point. The Newton update became bit-identical across 9 consecutive iterations and the residual stalled at 1.1251×10^{-6} against a convergence tolerance of 10^{-6} — close enough to look like an ordinary tolerance limitation, and stubborn enough to look fundamental.

It presented as a property of the discretisation: steps larger than 0.095 yr could never converge, however long they iterated. We first attributed that to the finite-difference Jacobian, whose perturbations were larger than the error-minimising step for a one-sided difference, so reducing them should have moved the wall. Across 7 combinations of the pressure and composition perturbations, spanning two orders of magnitude, the final residual was identical to the last bit; damping made no difference either. A quantity insensitive to every parameter that ought to control it is not a numerical limit but an algebraic constraint, and that is what located the clamp.

The cost did not register in any check: 29% of Newton attempts were discarded as failed steps, consuming 52% of wall-clock time, and the time-step controller was pinned below 0.095 yr for the whole run. Replacing the hard clamp with a tolerance of one part per million inside the loop, an exact projection applied once at commit time, and a counter of how many cells and how much mass are projected, gave 1.71× at matched step size and 3.24× with the controller free.

The reason for reporting this is not the speed-up. It is that throughout, every gate stayed green. The golden test passed, the verification suite passed, mass was conserved to 1.2×10^{-8} relative — better, in fact, than after the fix, where the larger steps the controller now takes raise the drift to 1.8×10^{-5}. A silent clamp does not corrupt results; it converts a modelling constraint into what appears to be a numerical one while every check reports normal. The defence that worked here was to make the clamp count what it clamps and report the count, which is what this code now does; whether the same guard pays off elsewhere depends on how common the situation is, which one code cannot estimate.

4.4 Measurement discipline and what survived it

Under the protocol of Section 3.4, 8 of 18 interventions survived isolated A/B measurement and 10 were rejected, the first of them two-stage constrained-pressure-residual preconditioning (Wallis, 1983; Wallis et al., 1985) — the standard recommendation for this class of system. Figure 6 plots the 14 with a representative paired ratio and Table 6 lists what each rejection measured; what follows is what the exercise taught rather than the ledger.

The acceptance rule matters most where two interventions have the same median. The uniform-axis table locate has a median of 1.07× over nine pairs spanning well below and well above one, and was rejected; the flat table gather has the same median, 1.07×, with every one of its five pairs above unity, and was adopted. We had used min-of-N first, on the usual argument that the fastest observation is the least polluted; on this machine a single anomalous sample inverted a result, reporting 0.89× where the paired median gives 1.45×. Pairing is what defends against a drifting clock rate; taking a minimum does not.

4 results initially came out with the wrong sign, and in each case the measurement had held fixed something the production run varies. A fixed-Δt microbenchmark reported 1.65× for reusing the preconditioner across time steps, where the real controller gives 0.89×: the

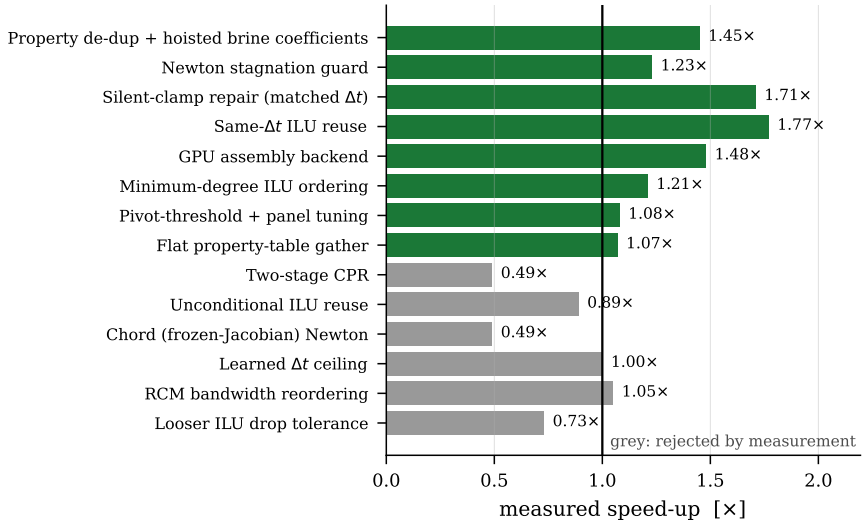

Figure 6: Measured speed-up of the 14 performance interventions that have a representative paired ratio; 4 further rejections lack one and are described in the text. Grey bars were rejected by measurement under the acceptance rule of Section 3.4.

accumulation block of the Jacobian scales as $1/\Delta t$, so a controller that changes Δt invalidates exactly what the microbenchmark held constant. Timing the linear solve with a warm factorisation cache hid a 3.94 s setup cost and inverted our diagnosis of where time was going. And at the coarser grid, single-shot timings reported 10 configurations as slower than the default; interleaved repetition showed every one of them faster. Not one row survived — the entire table had the wrong sign.

Regime matters as much as intervention. Our production runs pin the step size at an accuracy ceiling rather than letting the controller choose it, so the factorisation is reused across steps instead of rebuilt and assembly moves from 40% of a step to 58%. The same sparse-LU tuning is worth 1.36× under the free controller and 1.08× once the step is pinned, because what survives amortisation is the cheaper application of a reused factorisation, not the cheaper build. The GPU backend behaves the same way: 1.48× at the official grid, and on a 20,000-cell case under a direct solve, where the device cannot touch the dominant cost, 1.05× — with the ILUT variant of that case straddling unity, hence a rejection rather than a small win. Backend agreement is verified at field level rather than by summary statistics: after six identical controller steps at the official grid — identical also in their Newton-iteration and step-size trajectories — the pressure field agrees to 3×10^{-13} relative, the composition and saturation fields to 2×10^{-8}, and the Box A and B CO_2 inventories to 4×10^{-14}.

One rejection deserves separating out, because it resembles the intervention beside it and behaves in the opposite way. The incomplete factorisation dominates the linear solve — 93% of it at the official grid — and its cost is set by fill, so a bandwidth-reducing ordering ought to help. Reverse Cuthill–McKee narrows this Jacobian's bandwidth by 6.9× and returns 1.05×, while a minimum-degree ordering on $A^\top + A$ returns 1.21× with 38% fewer factorisation nonzeros. Bandwidth and fill are different objectives and only one is the cost here. What settles it is a control: the identity ordering fails outright, exactly singular at both grid sizes. The library is not indifferent to what it receives, so bandwidth reduction bought nothing because it optimises the wrong thing, not because ordering does not matter.

4.5 Spatial structure and cross-validation

The sparse time series are integrals; the dense maps show what produces them. We archived 200 maps at 5 yr intervals out to 1000 yr, the full length of the run (Fig. 7).

The clearest structure is the fate of the gas footprint after injection ends at 50 yr (Fig. 8). It does not freeze. The number of cells containing free gas keeps growing while the plume redistributes buoyantly, peaks at 10215 cells at 185 yr, and then declines to 7580 by 1000 yr — a 25.8% contraction at 343 cells per century, with only 6 upward excursions in the 163 intervals after the peak. Meanwhile the number of cells holding dissolved CO_2 without free gas rises to 57381 at 4723 cells per century, and the ratio of dissolved to gas-bearing cells reaches 7.57 at the end of the run, still rising. Dissolution consumes the free phase from the outside in: the halo grows at the footprint's expense, and both rates are close to constant over the second half of the millennium.

The length of the record decides that reading. Measured over any window that ends near the maximum, the same footprint count is flat by construction; the contraction and its rate only become visible once the archive extends well past 185 yr. A post-injection plume described as static is a statement about an observation window as much as about the physics.

Whether the dissolved halo sinks needs a metric that survives the domain's geometry. Dissolved mass below the *domain-wide* deepest gas-bearing cell sits near 1.6% with a flat trend (8.5×10^{-4} points per year), but the domain holds gas accumulations at two depths, so everything descending beneath the shallow crest accumulation while remaining above the deep one is invisible to that measure. The metric used here is local: for every column that holds gas, descent is measured against that column's own deepest gas cell, at two composition thresholds (10^{-6} and 10^{-4}).

The local metric changes the answer in two directions at once (Fig. 8, right). Through the first ∼335 yr it still shows no sustained descent: the below-interface fraction *falls* from its injection-era high to a minimum of 6.7% (4.6% at the stricter threshold), because the spreading gas cap advances over injection-sourced deep dissolved mass while dissolution adds mass at the interface. The early-time halo is a diffusive–dispersive skin of order one cell thick, consistent with the 10 m dispersivity the specification prescribes. From 335–340 yr — both thresholds date it identically — the fraction turns and rises at 0.016 points per year, reaching 18% (16.1%) by 1000 yr. The maps over the same interval develop vertically elongated dissolved structures in the water columns around the crest accumulation, and dissolved mass accumulates below the crest contact where no deeper gas body underlies it (Fig. 7, right). We identify this as the onset of density-driven convective redistribution of dissolved CO_2, resolved at this grid from 335–340 yr. Convective dissolution is the mechanism by which a dense CO_2-charged brine layer beneath the gas contact becomes gravitationally unstable and sinks; its onset time, wavelength and dissolution flux have been characterised theoretically and numerically for the single-contact configuration (Ennis-King and Paterson, 2005; Riaz et al., 2006; Hidalgo and Carrera, 2009; Slim, 2014; Emami-Meybodi et al., 2015). We do not claim that geometry here, because the domain holds gas at two depths and the descending transport organises around both. The depth tail is not the onset evidence: the 95th-percentile penetration below the local interface ends at 690 m (660 m at the stricter threshold) and grows at 0.43–0.43 m/yr, but that growth is confounded with the gas cap spreading over injection-sourced deep dissolved mass, so the diagnosis rests on the fraction metric and the map morphology. What these snapshots cannot do is exclude sub-grid fingering before the onset: the critical wavelength predicted for these conditions is well below our 10 m cell (Riaz et al., 2006; Pau et al., 2010), so a grid of this resolution registers convective transport only once it has organised into structures the grid can carry.

This also explains a quantity the coarse-grid runs got badly wrong. Immobile CO_2 in Box A is small because the gas front is sharp: at the final archived time 1620 cells carry gas saturation between 0.1 and 0.3 against 961 between 0.05 and 0.1, a ratio of 1.7: little of the domain sits in the partially-drained state where residual trapping accumulates.

As an independent check on the reporting pipeline, Box A inventories integrated from the dense maps agree with the sparse series, which a different code path computes: immobile CO_2

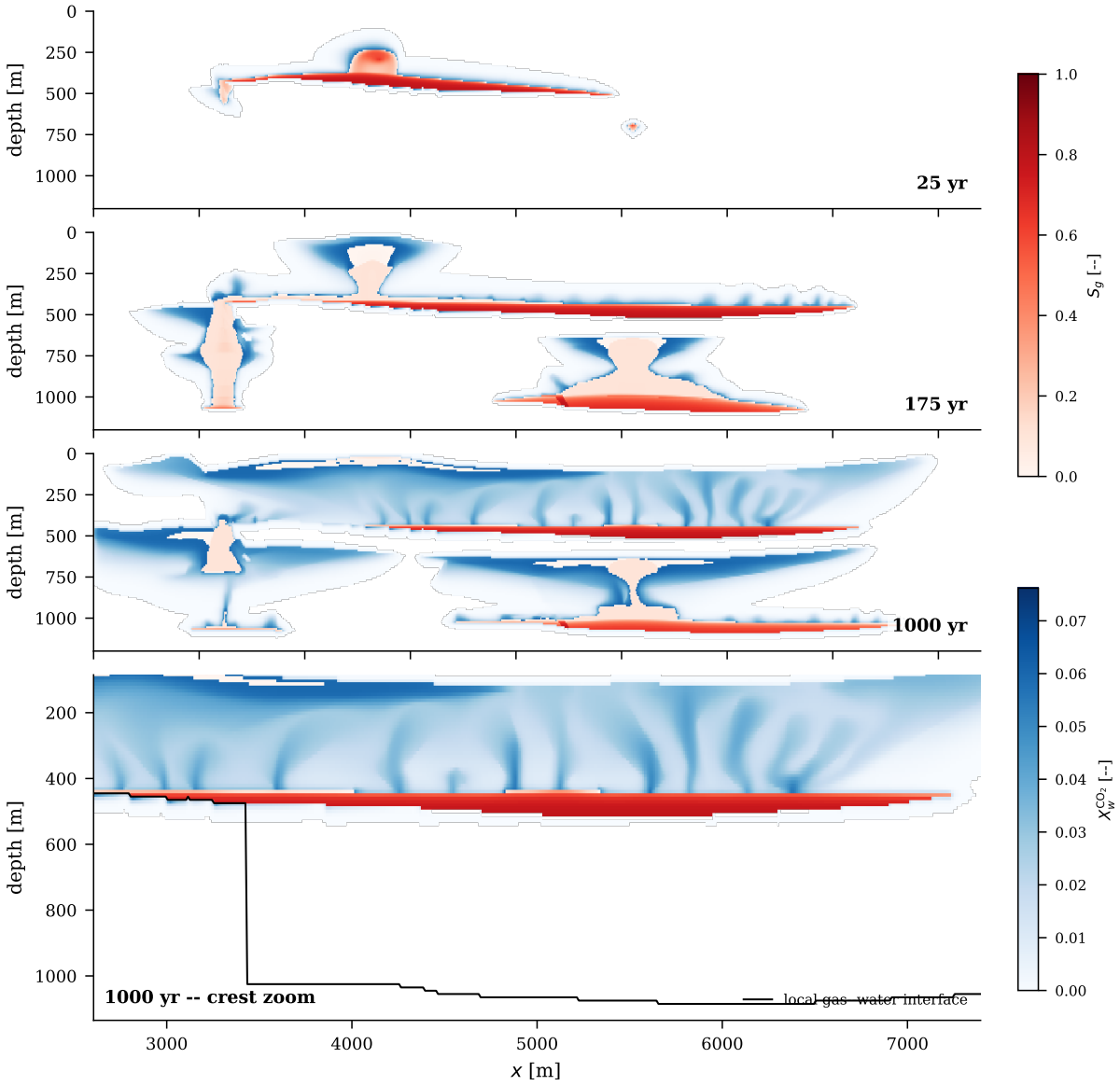

Figure 7: Free gas (S_g, red scale) and dissolved CO_2 ($X_w^{CO_2}$, blue scale) at three times, with the final panel enlarged around the crest accumulation; both fields are masked below 10^{-6}, the analysis threshold. The gas plume reaches the anticline crest and stops spreading; the dissolved halo first widens laterally, then develops the vertically elongated structures quantified in Fig. 8. The black curve in the enlargement is the per-column local gas–water interface used by that metric; its jump marks the domain's two gas bodies.

154.20 t against 155.93 t, a disagreement of 1.73 t, and mobile CO_2 to 0.04%. The same integration reproduces the prescribed injection schedule, giving a plateau of 82.81 kt.

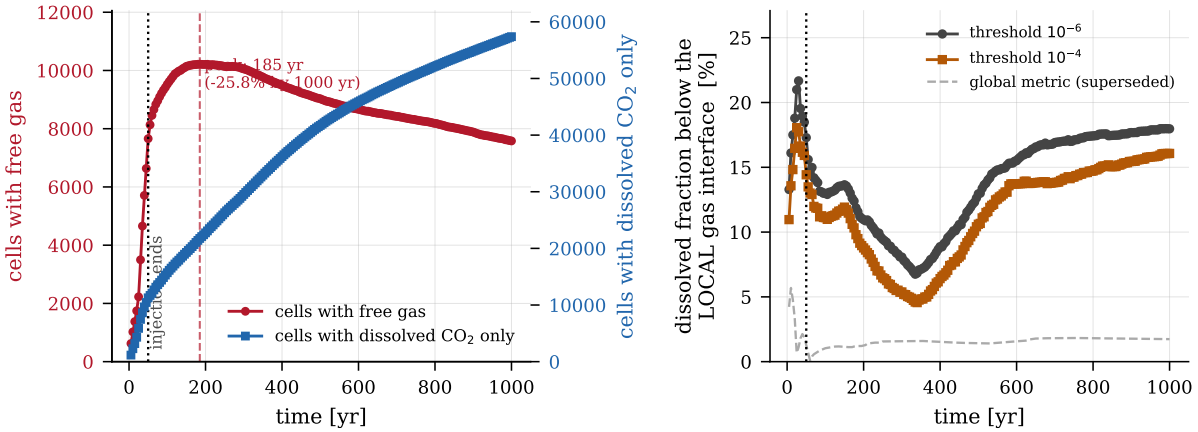

Figure 8: Left: cells containing free gas (marked at its peak) against cells containing only dissolved CO_2, on separate scales. Right: dissolved fraction below the local per-column gas interface at two thresholds, with the domain-global measure (grey dashes) that cannot see descent beneath the shallower of two gas bodies. The minimum at 335–340 yr dates the onset of resolved convective redistribution.

5 Results II: Sleipner

SPE11B is a controlled problem with a specification. This section applies the same discipline — explicit nulls, matched comparisons, stated limits — to the setting with no specification to conform to. The question changes accordingly, from "does the model match the specification" to "does the mechanism the model encodes account for what was observed". We use the Sleipner CO_2 injection site (Baklid et al., 1996; Arts et al., 2004), where repeated seismic surveys have mapped the plume since 1996 (Chadwick and Noy, 2010) and the 2019 Benchmark Model (Equinor, 2020) publishes interpreted layer outlines, a corner-point structural grid and the interpreted feeder chimney under a permissive licence. Flow models of the site span sharp-interface and vertical-equilibrium reductions (Nordbotten and Celia, 2011; Nilsen et al., 2016) and full multiphase history matches (Singh et al., 2010; Cavanagh and Haszeldine, 2014); what follows is neither, but a discrimination test among the reduced mechanisms those studies build on.

5.1 A footprint metric with a null model

We compare candidate mechanisms against the observed outline of the topmost sand layer, L9, on the benchmark model's own 50 m grid. The observed footprint covers 857 cells (2.14 km^2); agreement is measured by the Jaccard index, the intersection over the union of the two masks.

The design choice that matters is that every hypothesis is evaluated at *matched area*. Each candidate mask contains exactly as many cells as the observation, so no hypothesis can gain or lose by predicting the wrong amount of CO_2 — only by predicting it in the wrong place or the wrong shape. That makes room for a baseline carrying no mechanism beyond the two inputs every hypothesis gets: a radial disc of the same area centred on the interpreted feeder chimney. It is a strong baseline precisely because it is given the source location and the extent, and whatever a mechanism achieves it has to achieve against that.

Five hypotheses are compared (Fig. 9). Three are geometric limits, inexpensive enough to score exhaustively. The *up-dip decay* field is the simplest structural heuristic: mask thickness set by structural elevation relative to the feeder minus a decay with distance from it, with its single free parameter fitted to maximise its own score. *Invasion percolation* (Wilkinson and Willemsen, 1983) fills the structure from the feeder chimney under buoyancy and capillary entry pressure, the infinite-time limit of structural trapping. *Topographic fill* takes the shallowest cells and nothing else — structural control with no connectivity requirement, the limit in which the

Table 2: Overlap with the observed L9 outline, all hypotheses at matched area. The north–south to east–west aspect ratio is reported alongside because it shows that a high Jaccard score and reproducing the plume's shape are different achievements.

Hypothesis	Jaccard	N–S/E–W aspect
Observed L9 (reference)	1.000	3.04
Up-dip decay (best parameter)	0.351	1.25
Vertical-equilibrium sheet (best rate)	0.328	1.14
Radial disc (matched-area baseline)	*0.316*	*1.00*
Invasion percolation	0.187	2.35
Topographic fill	0.081	2.81

plume has fully equilibrated with the caprock relief. The fourth is a solved flow model: a *vertical-equilibrium sheet* (Nordbotten and Celia, 2006; Gasda et al., 2009) integrated over the layer, with Utsira permeability and porosity read from the benchmark model itself and thickness from its structural grid. It is advanced from the feeder until its own detectability footprint reaches the observed area — 8.4 yr at its most favourable rate, 0.018 m^3/s, matching that area to 1.8%. And the *radial disc* is the baseline. Each is granted its best case, so every score below is an upper bound on that hypothesis' skill here.

5.2 The mechanisms barely beat the baseline

Table 2 gives the result. The best hypothesis, up-dip decay at its most favourable parameter, reaches 0.351 against 0.316 for the baseline — 1.11× the baseline, or 0.035 in absolute overlap. The solved vertical-equilibrium sheet, the only hypothesis here that integrates a flow equation, scores 0.328: above the baseline, but by less than the heuristic that carries none of its physics, and with an aspect ratio of 1.14 against the observed 3.04 — the same too-isotropic failure as the disc. Rigidly shifting it over ±500 m raises it to 0.387, and its centroid sits 837 m from the observed one, south of it, so the sheet under-predicts the up-dip migration rather than misplacing it at random. The two structurally-driven mechanisms score *below* the baseline: invasion percolation 0.187 and topographic fill 0.081.

That ordering is the substantive result of this section. Adding real flow physics to a reduced model does not, here, buy overlap: the ranking of the five hypotheses is not the ranking of how much physics each contains.

Three supporting measurements make the negative result specific.

Structural control is not established at this resolution. Cells inside the outline are 1.20 m shallower than their 1 km neighbourhood ($r = +0.087$). A pointwise test reports $p = 4.4\times10^{-14}$, but that treats thousands of spatially correlated cells as independent replicates. Under a null that preserves that correlation — 999 toroidal shifts of the outline over the same relief, preserving both fields' autocorrelation — chance placements match or beat the observed correlation with $p = 0.078$, and the null's own 95th percentile (+0.094) exceeds the observation. Once spatial dependence is accounted for, the correlation therefore falls short of significance at 0.05: it is weak evidence for topographic control rather than none, and far from the near-zero p the pointwise test suggests. That is consistent with the failure of topographic fill, the mechanism that assumes structure is the whole story.

The plume is in a rate-limited transient. The observed centroid lies 776 m up-dip of the feeder chimney, whereas invasion percolation — the infinite-time filling limit — overshoots it by a further 1.5 km. The real plume has not finished migrating, so a model that assumes it has cannot place it correctly.

The mismatch is not registration error. Rigidly translating the invasion-percolation footprint over a ±500 m search improves its score only from 0.187 to 0.208. The failure is of shape,

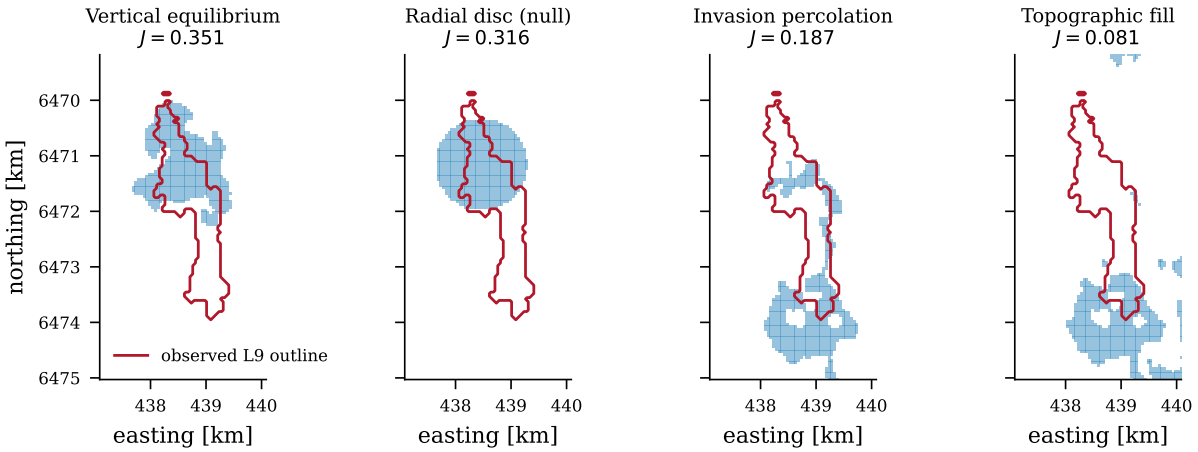

Figure 9: Four reduced models (blue) against the observed L9 outline (red), all at matched area on the benchmark model's 50 m grid. The best of them reaches 0.351; a radial disc of the same area centred on the interpreted feeder chimney, carrying no mechanism beyond those two inputs, reaches 0.316.

not of position.

The shape statistics in Table 2 sharpen this. The observed plume is strongly elongated north–south (aspect 3.04); the disc is by construction isotropic (1.00); invasion percolation and topographic fill do capture the elongation (2.35 and 2.81) and still score below the disc, because they place the elongated mass in the wrong position. A mechanism can get the shape right and the location wrong, and an overlap metric will — correctly — penalise that more than it penalises a circle in the right neighbourhood with no shape at all (Table 2).

5.3 What this does and does not show

This is hypothesis discrimination, not validation, and its evidential weight is bounded by four design choices. Every score is an *in-sample* best case — each hypothesis' free parameter is fitted on the footprint it is scored against, and with a single vintage no held-out assessment exists — so each is an upper bound, which strengthens the negative reading and forbids the positive one. The comparison covers one layer at one vintage on the benchmark model's 50 m grid. The observed outline is an interpreted product carrying digitisation and imaging uncertainty we cannot quantify, so the Jaccard values carry no error bars; the feeder location is itself an interpretation, probed only by the rigid ±500 m sweep; and a disc is one defensible baseline, not the only one. The vertical-equilibrium sheet is a sharp-interface reduction of one layer with a single source, not a history match: a full multiphase model of the whole stack (Singh et al., 2010; Cavanagh and Haszeldine, 2014) carries the feeder history and the intra-Utsira barriers it omits, and we make no claim about what such a model would score. The claim is narrower: the five explanations tested here, each at its best case and matched in area, exceed a circle by at most 0.035 in absolute overlap. What sets the footprint instead is not something this test can identify: an overlap statistic ranks candidate masks, it does not nominate the mechanism that would win. Cavanagh and Haszeldine (2014) argue on independent grounds for the history of flux through the feeder system and the intra-Utsira barriers, which every model tested here omits; our result is consistent with that and is not evidence for it.

We make no numerical comparison with published Sleipner history matches. Those studies report agreement through visual overlay of outlines, per-layer areas and time-lapse amplitude (Arts et al., 2004; Williams and Chadwick, 2012; Cavanagh and Haszeldine, 2014; Chadwick and Noy, 2010), not through a footprint-overlap statistic, so a claim that our $J = 0.351$ is better or worse than published work would be manufactured by the act of comparing. What is defensible, and what we report, is that the metric discriminates sharply between hypotheses

on real data, and that it does so only because the baseline is there to calibrate what a good score means. A Jaccard of 0.351 sounds respectable in isolation. Against 0.316 for a circle, it does not.

6 Discussion

6.1 The larger observed shifts are upstream of the numerics

On the controlled benchmark, where both axes were varied, conformance repair at fixed grids moved this run further than the full 5×-per-axis refinement ladder did at either stage (Section 4.1). The field case is weaker evidence for the same idea and should be read as such: Section 5 holds resolution fixed throughout, so it cannot weigh representation against resolution at all. What it does show is that five reduced models, each given its best case, separate from a matched-area baseline by no more than 1.11× — that is, which mechanism a model encodes mattered less to the observed footprint than having a baseline to measure it against.

What keeps that from being an argument the numbers do not support is that both discretisation effects sit inside measured floors — the 0.46 MAD produced by a change of time-step policy on identical physics, and the 0.06 MAD produced by a tenfold-finer injection step — while the conformance repairs do not. The ordering is also metric-dependent: under all thirteen reported quantities the coarse-grid pairing reverses (Appendix F), whereas the envelope result holds under both quantity sets because it does not average.

This is not an argument against mesh refinement, and the results do not support one: refinement helps over the whole ladder at both conformance stages, and mobile CO_2 in Box B is unresolvable on coarse grids at all (Section 4.2). The argument is about *where the next unit of effort goes, first* — and about what a benchmark exercise can attribute at all, given that a policy-dependent term of the same size as its reported effects can sit unstated inside any archive assembled as the work proceeds.

6.2 Verification cannot see conformance

The gap Section 3.2 names is not closable with more tests of the kind that missed the defects: a suite whose oracles share the code's reading of the specification will pass however strong it is otherwise. What closed it here was an itemised reading of the specification against the implementation, written down clause by clause. The SPE11 specification (Nordbotten et al., 2024) and its results paper (Flemisch et al., 2025a) ask participants to describe their setup, not to map each clause to the lines implementing it; we have not surveyed other exercises for such a requirement.

Benchmark exercises could ask participants to submit a conformance statement: for each numbered equation and table in the specification, the location in the code that implements it, and any deviation with its measured effect — the form of Table 1. Every defect reported here is of a kind such a statement would expose, each being a mismatch between a numbered clause and the lines implementing it rather than a subtle numerical issue. The cost is one reading of the specification against one's own code, and the result would convert inter-code spread from an unexplained distribution into something with attributable causes.

6.3 What a consensus metric rewards

Section 4.2.1 showed the same summary statistic moving against the bulk of its components twice, in opposite directions. Neither instance is a defect in the arithmetic; both are what a median over incommensurable entries does.

The consequence is that a consensus metric measures typicality, and optimising against it pulls submissions toward the group. Where the group shares a common bias — a correlation

everyone takes from the same source, a boundary treatment everyone inherits from the same lineage — that pull is toward the bias. Inter-code agreement is then evidence of shared ancestry rather than of correctness, and the agreement tightens with each round of the exercise. Whether the SPE11 pool has such shared lineages is testable from the submission archive and is not something this paper establishes.

The answer is not a different summary statistic; any aggregate over incommensurable quantities will have a pathology of this kind. Two responses cost little. Report the distribution rather than only its summary, as Fig. 4 does, so that a result which improves where it is worst is visible as such. And report a measure that cannot be improved by moving inward: envelope membership resolves less per pair than a distance does, but it cannot be improved by regression toward the group, which is why the conformance result is clearest under it.

6.4 Silent guards

Clipping a physically-bounded variable inside a nonlinear loop is a defensive measure that carries no diagnostic of its own. What Section 4.3 adds to that observation is that such a guard can convert a modelling constraint into an apparent numerical one while every gate reports normal — mass conservation included, at 1.2×10^{-8} relative. What generalises is not a frequency estimate, which one code cannot supply, but the symptom: a convergence limit that does not respond to any parameter that should control it, together with an update that is bit-identical across iterations rather than slowly shrinking. The defence is a clamp that counts what it moves and a run that reports the count.

6.5 Limitations

The simulator runs on structured grids, and the configuration reported here is two-dimensional; corner-point geometry is read for its properties but not used for the flow solution. That is what restricts the Sleipner work to the reduced-model comparison of Section 5, and it bounds the platform claim of Section 3.1: the capabilities of Table 8 are verified on structured grids at the scales stated there, not at field scale on industry geometry.

The mass-conservation audit sits at 1.8×10^{-5} relative in the production configuration. In absolute terms the denominator is the cumulative injected CO_2 (82.81 kt), so the end-of-run audit corresponds to 1.5 t of CO_2 — the same order as the 1.73 t disagreement between the sparse and dense estimates of Box A immobile mass in Section 4.5, which calibrates what mass statements at that scale can mean. Under a sweep of step sizes the audit behaves as a random walk rather than a systematic drift, ranging over two orders of magnitude with no monotone trend, so its *scale* is controllable but its value at the end of a run is not. We report the value rather than the best value we could obtain by choosing the run.

The specification review was performed by the same person who wrote the code. It found 7 defects the tests could not, but a single reader can also reproduce their own interpretation of an ambiguous clause, so its completeness is not established — only its yield. The itemised clause-to-code table exists precisely so that a second, independent reading can be performed without re-deriving the mapping; such a re-reading would be the most valuable external check on this work.

The grid-by-stage matrix is complete, but its axes are not sampled equally: four grids against two conformance stages. The stage effect is therefore measured at four resolutions, while what a finer grid does to the value of the specification review rests on those two stages alone. The Sleipner comparison is of reduced models at a single layer and vintage: it establishes that these mechanisms do not separate from a matched-area baseline, not what would. And one deviation from the specification (D7) was measured and kept, at 2.8×10^{-7} of the domain CO_2 inventory.

7 Conclusions

We built a CO_2 storage simulator from scratch, ran it on SPE11B at the specification's own reporting resolution, and positioned it against the archived submissions. The final placement — rank 15 of 33 under this paper's consensus distance, 19 of 33 under the published SPE11 measure, and 53 of 54 sampled quantity–time pairs inside the peer envelope — lies within the peer spread. How it was reached is the subject of this paper, and the eight contributions promised in Section 1 resolve as follows.

1. **Specification conformance moved this run further than grid refinement did, and the two are now separated rather than confounded.** Repairing 6 defects at fixed grids moved envelope membership by 9 and 10 of 54 pairs, and the consensus distance by 1.85 and 0.72 MAD. The full 5×-per-axis refinement ladder moved it by 0.8 at D1–D5 and 0.46 at D1–D6. With both conformance stages run at all four grids, the largest per-quantity stage effect falls monotonically from 0.88 to 0.03 MAD as the grid refines, and its aggregate ends at -0.01 MAD at the reporting grid after changing sign twice on the way. The deterioration an earlier reading of the two finest runs attributed to resolution therefore decomposes into a stage cost of +0.08 and a matched-refinement gain of 0.04.

2. **Comparison measures need their own reproducibility and their own pathologies reported.** Identical physics rerun under a different time-step policy moves the nine-quantity aggregate by 0.46 MAD, and a tenfold-finer injection time step moves it by 0.06 MAD — more than the 0.04 that the finest refinement buys. Both are carried by the one quantity whose absolute masses make its scaled deviation quantisation noise. Separately, the median aggregate moved against the bulk of its components twice, with opposite signs. Refinement claims of this size are uninterpretable without such floors beside them, and consensus scores should be published with their distributions.

3. **Code-verification tests do not establish specification conformance when their oracles share the implementation's reading of the specification.** All 7 defects survived 42 test groups and 465 assertions. Independently derived oracles, prescribed benchmark invariants, or a second reader can detect such defects; more tests of the same lineage cannot. An itemised clause-to-code statement is what found them here, and is what a benchmark exercise could ask for.

4. **A silent clamp can present as a convergence limit.** One line clipping a bounded variable inside the Newton loop capped the time step at 0.095 yr and consumed 52% of wall-clock time in discarded iterations, while every gate stayed green. It has a distinctive signature (Section 6.4), and the defence that worked was to make the clamp count what it clamps.

5. **Most performance intuitions did not survive measurement.** 8 of 18 interventions were kept; 4 first reported the wrong sign, in every case because the benchmark held fixed something the production run varies. The acceptance rule that separates them — every paired ratio above unity — also rejects one configuration whose median alone would have passed, and the accepted device gain is regime-dependent rather than absolute.

6. **The free-gas footprint does not freeze when injection stops.** Over the full 1,000 yr record it peaks at 10215 cells at 185 yr and then contracts by 25.8%, while the dissolved region keeps growing; a per-column interface metric dates resolved convective redistribution from 335–340 yr. Measured over any window ending near the peak, the same count reads as static — the reading depends on the length of the record.

7. **The simulator is verified beyond what this problem exercises.** The 9144-line core implements the capabilities of Table 8, each gated against an analytical or published reference solution, of which SPE11B exercises the flow, transport and constitutive subset. That is what makes the conformance finding interpretable: the defects survived a suite that was strong, not a suite that was thin.

8. **On a field case, reduced models barely beat a baseline.** Against the observed Sleipner L9 outline at matched area, the best hypothesis reached 0.351 and a solved vertical-equilibrium sheet 0.328, against 0.316 for a disc of equal area centred on the interpreted feeder. The ordering of the five hypotheses is not the ordering of how much physics each contains. Reduced-model agreement is uninterpretable without an explicit baseline.

The connecting claim rests on the benchmark study, where both axes were varied: the larger observed discrepancy shifts originated upstream of the discretisation, in what the model was asked to represent and in the assumptions that survive unexamined because every check reports normal. The field case, at fixed resolution, adds only that reduced-model agreement is uninterpretable without a baseline. A comparative solution project is well placed to expose the first of those, and could do so by asking participants to state their conformance and show where it was checked.

References

R. Arts, O. Eiken, A. Chadwick, P. Zweigel, L. van der Meer, and B. Zinszner. Monitoring of CO_2 injected at Sleipner using time-lapse seismic data. *Energy*, 29(9–10):1383–1392, 2004. doi: 10.1016/j.energy.2004.03.072.

Khalid Aziz and Antonin Settari. *Petroleum Reservoir Simulation*. Applied Science Publishers, London, 1979.

Alan Baklid, Ragnhild Korbøl, and Geir Owren. Sleipner Vest CO_2 disposal, CO_2 injection into a shallow underground aquifer. In *SPE Annual Technical Conference and Exhibition*, 1996. doi: 10.2118/36600-MS.

Michael Batzle and Zhijing Wang. Seismic properties of pore fluids. *Geophysics*, 57(11):1396–1408, 1992. doi: 10.1190/1.1443207.

Royal H. Brooks and Arthur T. Corey. Hydraulic properties of porous media. Hydrology Paper 3, Colorado State University, Fort Collins, Colorado, 1964.

Andrew J. Cavanagh and R. Stuart Haszeldine. The Sleipner storage site: Capillary flow modeling of a layered CO_2 plume requires fractured shale barriers within the Utsira Formation. *International Journal of Greenhouse Gas Control*, 21:101–112, 2014. doi: 10.1016/j.ijggc.2013.11.017.

R. A. Chadwick and D. J. Noy. History-matching flow simulations and time-lapse seismic data from the Sleipner CO_2 plume. *Geological Society, London, Petroleum Geology Conference Series*, 7:1171–1182, 2010. doi: 10.1144/0071171.

Jon F. Claerbout and Martin Karrenbach. Electronic documents give reproducible research a new meaning. In *SEG Technical Program Expanded Abstracts*, pages 601–604, 1992. doi: 10.1190/1.1822162.

Holger Class, Anozie Ebigbo, Rainer Helmig, Helge K. Dahle, Jan M. Nordbotten, Michael A. Celia, Pascal Audigane, Melanie Darcis, Jonathan Ennis-King, Yaqing Fan, Bernd Flemisch, Sarah E. Gasda, Min Jin, Stefanie Krug, Diane Labregere, Ali Naderi Beni, Rajesh J. Pawar, Adil Sbai, Sunil G. Thomas, Laurent Trenty, and Lingli Wei. A benchmark study on problems related to CO_2 storage in geologic formations. *Computational Geosciences*, 13(4):409–434, 2009. doi: 10.1007/s10596-009-9146-x.

Keith H. Coats. An equation of state compositional model. *Society of Petroleum Engineers Journal*, 20(5):363–376, 1980. doi: 10.2118/8284-PA.

David L. Donoho. An invitation to reproducible computational research. *Biostatistics*, 11(3): 385–388, 2010. doi: 10.1093/biostatistics/kxq028.

Hamid Emami-Meybodi, Hassan Hassanzadeh, Christopher P. Green, and Jonathan Ennis-King. Convective dissolution of CO_2 in saline aquifers: Progress in modeling and experiments. *International Journal of Greenhouse Gas Control*, 40:238–266, 2015. doi: 10.1016/j.ijggc.2015.04.003.

Jonathan Ennis-King and Lincoln Paterson. Role of convective mixing in the long-term storage of carbon dioxide in deep saline formations. *SPE Journal*, 10(3):349–356, 2005. doi: 10.2118/84344-PA.

Equinor. Sleipner 2019 Benchmark Model, 2020. Sleipner CO_2 Reference Dataset Licence.

A. Fenghour, William A. Wakeham, and V. Vesovic. The viscosity of carbon dioxide. *Journal of Physical and Chemical Reference Data*, 27(1):31–44, 1998. doi: 10.1063/1.556013.

Bernd Flemisch, Jan M. Nordbotten, Martin A. Fernø, Knut-Andreas Lie, Anthony R. Kovscek, et al. Benchmarking CO_2 storage simulations: Results from the 11th Society of Petroleum Engineers comparative solution project. *International Journal of Greenhouse Gas Control*, 148:104519, 2025a. doi: 10.1016/j.ijggc.2025.104519.

Bernd Flemisch, Jan Martin Nordbotten, Martin Fernø, Knut-Andreas Lie, Anthony Kovscek, et al. The 11th SPE comparative solution project: Submitted data, 2025b.

Julio E. García. Density of aqueous solutions of CO_2. Technical report, Lawrence Berkeley National Laboratory, 2001.

Sarah E. Gasda, Jan M. Nordbotten, and Michael A. Celia. Vertical equilibrium with subscale analytical methods for geological CO_2 sequestration. *Computational Geosciences*, 13 (4):469–481, 2009. doi: 10.1007/s10596-009-9138-x.

Juan J. Hidalgo and Jesús Carrera. Effect of dispersion on the onset of convection during CO_2 sequestration. *Journal of Fluid Mechanics*, 640:441–452, 2009. doi: 10.1017/S0022112009991480.

Herbert E. Huppert and Andrew W. Woods. Gravity-driven flows in porous layers. *Journal of Fluid Mechanics*, 292:55–69, 1995. doi: 10.1017/S0022112095001431.

John E. Killough. Reservoir simulation with history-dependent saturation functions. *Society of Petroleum Engineers Journal*, 16(1):37–48, 1976. doi: 10.2118/5106-PA.

Carlon S. Land. Calculation of imbibition relative permeability for two- and three-phase flow from rock properties. *Society of Petroleum Engineers Journal*, 8(2):149–156, 1968. doi: 10.2118/1942-PA.

David Landa-Marbán, Knut-Andreas Lie, Kjetil Olsen Lye, Olav Møyner, Atgeirr F. Rasmussen, and Tor Harald Sandve. Exploring convergence and its limits in Case B of the 11th SPE comparative solution project. *SPE Journal*, 31(3):2005–2016, 2026. doi: 10.2118/231853-PA.

Halvor Møll Nilsen, Knut-Andreas Lie, and Odd Andersen. Robust simulation of sharp-interface models for fast estimation of CO_2 trapping capacity in large-scale aquifer systems. *Computational Geosciences*, 20(1):93–113, 2016. doi: 10.1007/s10596-015-9549-9.

Jan M. Nordbotten and Michael A. Celia. Similarity solutions for fluid injection into confined aquifers. *Journal of Fluid Mechanics*, 561:307–327, 2006. doi: 10.1017/S0022112006000802.

Jan M. Nordbotten and Michael A. Celia. *Geological Storage of CO_2: Modeling Approaches for Large-Scale Simulation*. Wiley, Hoboken, NJ, 2011. doi: 10.1002/9781118137086.

Jan M. Nordbotten, Martin A. Fernø, Bernd Flemisch, Anthony R. Kovscek, and Knut-Andreas Lie. The 11th Society of Petroleum Engineers comparative solution project: Problem definition. *SPE Journal*, 29(5):2507–2524, 2024. doi: 10.2118/218015-PA.

William L. Oberkampf and Timothy G. Trucano. Verification and validation in computational fluid dynamics. *Progress in Aerospace Sciences*, 38(3):209–272, 2002. doi: 10.1016/S0376-0421(02)00005-2.

James L. Palandri and Yousif K. Kharaka. A compilation of rate parameters of water-mineral interaction kinetics for application to geochemical modeling. Open-File Report 2004-1068, U.S. Geological Survey, 2004.

George S. H. Pau, John B. Bell, Karsten Pruess, Ann S. Almgren, Michael J. Lijewski, and Keni Zhang. High-resolution simulation and characterization of density-driven flow in CO_2 storage in saline aquifers. *Advances in Water Resources*, 33(4):443–455, 2010. doi: 10.1016/j.advwatres.2010.01.009.

Donald W. Peaceman. Interpretation of well-block pressures in numerical reservoir simulation. *Society of Petroleum Engineers Journal*, 18(3):183–194, 1978. doi: 10.2118/6893-PA.

Roger D. Peng. Reproducible research in computational science. *Science*, 334(6060):1226–1227, 2011. doi: 10.1126/science.1213847.

Karsten Pruess, Curtis M. Oldenburg, and George J. Moridis. TOUGH2 user's guide, version 2. Technical report, Lawrence Berkeley National Laboratory, 1999.

A. Riaz, M. Hesse, H. A. Tchelepi, and F. M. Orr. Onset of convection in a gravitationally unstable diffusive boundary layer in porous media. *Journal of Fluid Mechanics*, 548:87–111, 2006. doi: 10.1017/S0022112005007494.

Patrick J. Roache. Perspective: A method for uniform reporting of grid refinement studies. *Journal of Fluids Engineering*, 116(3):405–413, 1994. doi: 10.1115/1.2910291.

Christopher J. Roy and William L. Oberkampf. A comprehensive framework for verification, validation, and uncertainty quantification in scientific computing. *Computer Methods in Applied Mechanics and Engineering*, 200(25–28):2131–2144, 2011. doi: 10.1016/j.cma.2011.03.016.

Youcef Saad and Martin H. Schultz. GMRES: A generalized minimal residual algorithm for solving nonsymmetric linear systems. *SIAM Journal on Scientific and Statistical Computing*, 7(3):856–869, 1986. doi: 10.1137/0907058.

Yousef Saad. ILUT: A dual threshold incomplete LU factorization. *Numerical Linear Algebra with Applications*, 1(4):387–402, 1994. doi: 10.1002/nla.1680010405.

Varunendra Singh, Andrew Cavanagh, Hilde Hansen, Bamshad Nazarian, Martin Iding, and Philip Ringrose. Reservoir modeling of CO_2 plume behavior calibrated against monitoring data from Sleipner, Norway. In *SPE Annual Technical Conference and Exhibition, Florence*, 2010. doi: 10.2118/134891-MS.

Anja C. Slim. Solutal-convection regimes in a two-dimensional porous medium. *Journal of Fluid Mechanics*, 741:461–491, 2014. doi: 10.1017/jfm.2013.673.

Roland Span and Wolfgang Wagner. A new equation of state for carbon dioxide covering the fluid region from the triple-point temperature to 1100 K at pressures up to 800 MPa. *Journal of Physical and Chemical Reference Data*, 25(6):1509–1596, 1996. doi: 10.1063/1.555991.

Nicolas Spycher, Karsten Pruess, and Jonathan Ennis-King. CO_2–H_2O mixtures in the geological sequestration of CO_2. I. Assessment and calculation of mutual solubilities from 12 to 100°c and up to 600 bar. *Geochimica et Cosmochimica Acta*, 67(16):3015–3031, 2003. doi: 10.1016/S0016-7037(03)00273-4.

A. Verma and Karsten Pruess. Thermohydrological conditions and silica redistribution near high-level nuclear wastes emplaced in saturated geological formations. *Journal of Geophysical Research: Solid Earth*, 93(B2):1159–1173, 1988. doi: 10.1029/JB093iB02p01159.

J. R. Wallis. Incomplete Gaussian elimination as a preconditioning for generalized conjugate gradient acceleration. In *SPE Reservoir Simulation Symposium, San Francisco*, 1983. doi: 10.2118/12265-MS.

J. R. Wallis, R. P. Kendall, and T. E. Little. Constrained residual acceleration of conjugate residual methods. In *SPE Reservoir Simulation Symposium*, Dallas, Texas, 1985. doi: 10.2118/13536-MS.

D. Wilkinson and J. F. Willemsen. Invasion percolation: a new form of percolation theory. *Journal of Physics A: Mathematical and General*, 16(14):3365–3376, 1983. doi: 10.1088/0305-4470/16/14/028.

Gareth Williams and Andrew Chadwick. Quantitative seismic analysis of a thin layer of CO_2 in the Sleipner injection plume. *Geophysics*, 77(6):R245–R256, 2012. doi: 10.1190/geo2011-0449.1.

A Verification depth

Table 3 lists the classes of check that make up the 465 assertions of Section 3.3. It is included because the central claim of Section 3.2 — that this suite could not detect any of the 7 conformance defects — is only meaningful if the reader can see that the suite is not weak.

B The evaluation trajectory in full

Table 4 gives every configuration behind Fig. 3. Ranks and distances are recomputed from the archived submissions each time the manuscript is built; they are not transcribed.

Table 3: What the verification suite checks, and against what. Every class listed was passing while all 7 conformance defects of Table 1 were present.

Class	Reference
Hydrostatic no-flow	machine precision: a gravitationally equilibrated column must produce no velocity
Buckley–Leverett	the analytical saturation profile for one-dimensional immiscible displacement
Aquifer response	the analytical pressure transient for a bounded aquifer
Conservation	component mass balance over every step, audited cumulatively
Restart	bit-exact state reproduction across a checkpoint boundary
Golden replay	every state variable against a stored reference at $r_{\mathrm{tol}} = 10^{-9}$
Geometry	facies assignment against the benchmark's reference map, all 100800 cells
Evaluation pipeline	the whole conformance trajectory of Section 4.1, recomputed from the archived submissions rather than stored
Benchmark invariants	the specification's own inventory identity, mobile + immobile + dissolved = total, per reporting box

Table 4: Every configuration run. Rank is among 33 entries (32 archived peers plus this work) under the nine-quantity metric of Eq. (1); the last two columns repeat rank and distance under the full thirteen reported quantities; envelope is the count of 54 sampled quantity–time pairs inside the peer min–max range. Rows marked † predate the current time-step policy, whose effect on identical physics is 0.46 MAD on the nine-quantity aggregate and 0.01 MAD excluding `immA` (Section 4.1); comparisons in the text are drawn within a policy where the distinction matters. The grid-by-stage matrix is complete: both conformance stages exist at all four grids. All values are recomputed from the archived submissions each time the manuscript is built.

		nine quantities			thirteen	
Grid	Conformance stage	Rank	Distance	Envelope	Rank	Distance
168×24	before the audit†	28	3.24	38	25	2.05
336×48	before the audit†	27	2.25	42	27	2.62
168×24	D1–D5 repaired†	24	1.73	47	25	1.85
336×48	D1–D5 repaired†	23	1.45	52	20	1.15
672×96	D1–D5 repaired†	14	0.89	53	13	0.95
840×120	D1–D5 repaired	15	0.94	53	13	0.96
168×24	D1–D6 repaired†	22	1.39	47	25	1.72
336×48	D1–D6 repaired†	24	1.53	52	21	1.26
672×96	D1–D6 repaired	16	0.97	54	13	0.98
840×120	**D1–D6 repaired**	**15**	**0.93**	**53**	**13**	**0.97**

C Sleipner reduced-model definitions

For reproducibility of Section 5: all masks live on the benchmark model's own 50 m grid, and every hypothesis mask is matched in area to the rasterised observed outline (857 cells) *after* rasterisation, by taking the top-N cells of the hypothesis' scalar field. The aspect ratio is the ratio of the mask's bounding-box extents, north–south over east–west. The up-dip decay field is structural elevation relative to the feeder minus λ times distance from it; λ is fitted in-sample

over $\{0\}$ and forty log-spaced values in $[10^{-5}, 10^{-1}]$, best at 3.1×10^{-2}. The vertical-equilibrium sheet is the solver gated against the Huppert and Woods (1995) $t^{1/3}$ scaling in Table 8. It runs on the same grid, taking the layer's permeability and porosity from the benchmark model and its thickness from the structural grid. Its free parameter is the source rate, swept until the footprint above a 0.5 m thickness threshold reaches the observed area; the overlap is flat to within 0.004 over 0.015–0.032 m^3/s. Invasion percolation floods from the feeder cell with uniform entry pressure, porosity and residual saturation and a buoyancy contrast of 320 kg/m^3, to the same pore volume the observed area implies. The null disc is centred on the feeder cell with radius 826 m (equal area). The feeder is mapped to the nearest cell centre of its interpreted centroid; the ±500 m registration sweep translates masks rigidly on the grid.

D Measurement environment and statistics

All wall-clock measurements were taken on one machine: an 12th Gen Intel(R) Core(TM) i9-12950HX (24 hardware threads), 63 GiB of RAM, and an NVIDIA RTX A2000 Laptop GPU (CUDA 12.9, CuPy 14.0.1), running Linux-7.0.0-28-generic-x86_64-with-glibc2.39 with Python 3.13.0, NumPy 2.2.6 (OpenBLAS) and SciPy 1.15.2. All arithmetic is IEEE double precision. GPU timings include host–device transfers and synchronise before every timer read; each A/B alternates its arms in one process (or in alternating subprocesses where the backend is chosen at import), with every long-running production job suspended for the duration. The absolute costs the text quotes come from the same setting, and unlike the paired ratios below they are single unreplicated runs. A full 1,000 yr run takes 251 s at 168×24 and 23.4 h at 672×96 over 9194 steps; a step at the official grid costs 5.48 s, of which assembly is 40% and the incomplete factorisation 3.94 s. Treat them as the order of the cost, not as figures repeatable to the quoted precision — the same case has measured 23 s and 35 s per step on this machine under different CPU governor states, which is why every comparative claim in Section 4.4 is a paired ratio instead.

Table 5 lists the deciding runs whose individual pairs were archived, under the acceptance rule of Section 3.4. Two of its rows concern the performance gate's own twenty-thousand-cell case rather than SPE11B, where the direct solve is 2.6× slower than ILUT on identical geometry — so the gate times the slower configuration.

The four sparse-LU settings of Section 4.4, each measured against this Jacobian rather than assumed: column ordering (minimum degree on $A^\top + A$, worth 1.25× in a per-timestep cost model), the diagonal pivot threshold and panel size (together 1.47× on the official-grid Jacobian in isolation), and the drop tolerance and fill factor, whose optima were re-swept under the new ordering and did not move.

Table 5: Paired-ratio statistics of the deciding A/B run for each intervention whose individual pairs were archived. N is the number of alternating pairs; the range is min–max over pairs. Entries are emitted from `paper/facts_measured.json` by the fact generator, not transcribed.

Deciding A/B run	N	median	range
Property de-dup + brine hoist	9	1.45×	not archived
Minimum-degree ILU ordering	3	1.21×	1.15–1.22
Pivot/panel tuning (free Δt)	3	1.36×	1.22–1.45
Pivot/panel tuning (pinned Δt)	3	1.08×	1.08–1.14
GPU backend (840×120)	2	1.48×	1.38–1.59
GPU backend (336×48)	3	1.40×	1.33–1.42
GPU backend, direct-solver case	3	1.05×	1.04–1.07
GPU backend, ILUT case (20k cells)	3	1.03×	0.96–1.08
Flat property-table gather	5	1.07×	1.05–1.09
Uniform-axis locate (rejected)	9	1.07×	0.56–1.34

Table 6 is the rest of the ledger: every intervention that measurement rejected, with what it measured. They are reported because a record of what did not work is the part of an optimisation history that goes unreported.

Table 6: The 10 rejected interventions. A ratio below unity is a slowdown; 1.00 means the effect vanished once an accuracy guard was attached. The last three had no single representative ratio and were bounded instead.

Intervention	Ratio	What it measured
Two-stage CPR	0.49×	14.7 s against 7.0 s for the incumbent ILUT–GMRES on the same system
Chord (frozen-Jacobian) Newton	0.49×	the iteration count rose *and* factorisations rose from one to 25 over the sampled window
Unconditional preconditioner reuse	0.89×	against 1.77× when restricted to steps where Δt is unchanged; the accumulation block scales as $1/\Delta t$
Learned Δt ceiling	1.00×	the gain vanished once an accuracy guard was attached
RCM bandwidth reordering	1.05×	bandwidth cut 6.9×; fill, not bandwidth, is the cost
Looser ILU drop tolerance	0.73×	re-swept under the new ordering; the optimum did not move
Uniform-axis table locate	1.07×	median over nine pairs, range straddling unity; bit-identical on every node before timing
GPU backend, ILUT case	1.03×	20,000 cells; paired range straddles unity
Tightened Newton tolerance	—	indistinguishable from run-to-run scatter
Dense-map output format	—	minutes against a run of 23.4 h
Thermal CSR pattern cache	—	bounded below 0.26% of a timestep

E Per-defect sensitivity battery

Each battery run re-introduces one reconstructed defect at 168×24 against a baseline rerun under today's runner and time-step policy; Section 4.1 gives the reading. The full nine-quantity aggregate is dominated at this grid by `immA`, for the reason given in Section 4.1, so the `immA`-excluded column carries the interpretable attribution.

Table 7: Consensus distance with ONE reconstructed defect re-introduced, against the matched-policy baseline (nine-quantity distance 1.85; `immA`-excluded 1.53, agreeing with the archived D1–D6 run's 1.54). The five excluded-aggregate deltas sum to +0.03 while the bundled repairs moved this grid by 1.85: the items interact.

	nine quantities		excl. `immA`	
Re-introduced defect	dist	Δ	dist	Δ
D1 k_{rg} normalisation	1.4	-0.44	1.17	-0.36
D2 p_c cap not enforced	1.85	+0.00	1.53	+0.00
D3 k_z isotropic	1.96	+0.12	1.98	+0.46
D4 κ single scalar	1.55	-0.29	1.47	-0.06
D5 mobility classification	1.93	+0.08	1.52	-0.01

F Quantity-set robustness across the trajectory

Section 2.2 justifies the nine-quantity metric and reports its effect on the final position. Two results are stable under the full thirteen-column set: the shape of the trajectory (the audit moves configurations up; refinement moves them up) and the sign structure of the D6 stage change (it worsens the mid grid by +0.11 under thirteen as under nine). One thing is not: the *relative magnitudes*, where the conformance-over-refinement ordering reverses at the coarse pairing. Under thirteen series the coarse-grid conformance delta shrinks to 0.33 MAD while the D1–D5 refinement ladder yields 0.9, reversing the nine-quantity ordering at that pairing. The mechanism is the one that motivated the exclusions (Section 2.2): the added series change little across peers, so they dilute the entries in which the review's largest repair — the Box A mobility classification — lives. The magnitude comparison between conformance and refinement is therefore a statement *about the nine-quantity metric*, and the main text says so where it makes it.

The per-configuration values under both quantity sets are in Table 4.

G Simulator capabilities and their reference solutions

The results of this paper come from the flow, transport and constitutive components of the core listed below. The same core carries the remaining capabilities, each held to an analytical or published reference solution; they are listed because the instrument's scope bears on what its verification record means, and marked so that no claim here is read as covering a component SPE11B does not exercise. Every reference solution named is a gate in the suite counted in Section 3.3.

Table 8: Capabilities of the simulator core, their verification oracles, and whether SPE11B as run here exercises them. "Machine precision" means the residual is at the level of floating-point round-off for the stated field.

Capability	Reference solution used as its gate	Here
Two-phase two-component flow	hydrostatic no-flow to machine precision; Buckley–Leverett front via the Welge tangent construction	yes
Primary-variable switching	component-mass conservation across every appearance, disappearance and dry-out transition	yes
Phase equilibrium and properties	Spycher et al. (2003) mutual solubility; Span and Wagner (1996) CO_2 equation of state; Batzle and Wang (1992) brine density	yes
Relative permeability, capillarity, regional parameters	the specification's own eqs. (2.6)–(2.9) and Table 4, reproduced cell by cell	yes
Trapping hysteresis	Land (1968) and Killough (1976) scanning curves; excluded by the SPE11 specification	no
Dispersion	the Ogata–Banks solution, by a difference design that cancels numerical dispersion	yes
Jacobian and linear solvers	full finite-difference Jacobian comparison; counted solver fallbacks	yes
Restart	bit-identical resume from checkpoint	yes
Energy equation	complementary-error-function conduction; Joule–Thomson enthalpy conservation	no
Reactive transport and mineral kinetics	independent carbonate-equilibrium root solve; Palandri and Kharaka (2004) rate laws	no
Poromechanics	Terzaghi consolidation and the Mandel–Cryer effect	no
Halite precipitation	Verma and Pruess (1988) permeability reduction	no
Dual-porosity transfer	analytical inter-continuum transfer time constant	no
Vertical-equilibrium reduction	the Huppert and Woods (1995) $t^{1/3}$ gravity-current scaling	§5
Analytical aquifer	the Fetkovich closed-form response	no
Ensembles and data assimilation	the exact Kalman posterior for a linear-Gaussian case	no
GPU backend	field-level agreement with the CPU path (Section 4.4)	yes